GEOPHYSICS, VOL. 74, NO. 4 (JULY-AUGUST 2009); P. E181–E191, 17 FIGS., 3 TABLES.
10.1190/1.3137060

An experimental study of the dilation factor

Arpita Pal Bathija[1], Michael Lee Batzle[1], and Manika Prasad[2]

ABSTRACT

Dilation factor R is the ratio of relative change in velocity to relative change in deformation (strain). It has significant implications for 4D seismic studies where it can be used to infer reservoir or overburden thickness changes from seismic changes, but the effect of stress on R and its components is not well understood. We conduct static strain and ultrasonic velocity measurements to study the effect of stress on R and its components. Measured absolute R values (6–91 in sandstones and 6–11 in shale) depend on the deformation mechanisms causing the strain. The dynamic (low-amplitude) Young's modulus generally is higher than the static (high-amplitude) Young's modulus. Hence, theoretical models that use the same mechanism to describe wave propagation and macroscopic deformation are invalid. The ratio of dynamic to static modulus depends on the direction of stress applied with respect to the density and placement of cracks. Values of R differ for P- and S-waves, especially in the presence of fluids. The values also depend strongly on the stress states; hence, using a constant value of R from the surface to reservoir depth should be avoided. Absolute R values increase for sandstones and decrease for shales with decreasing confining pressure, which explains the low R values from 4D seismic data. Our data offer insight into the behavior of R values with different rock types, stress, and fluid, and they can be used to constrain model calculations.

INTRODUCTION

Dilation factor R is defined as the ratio of the relative change in velocity to strain, where relative velocity change is the ratio of the change in velocity to initial velocity. It is used in time-lapse (4D) seismic studies to infer reservoir or overburden thickness changes from seismic changes. Detecting geomechanical changes to predict well failure or borehole stability and to monitor reservoir depletion opens up new ways of using 4D data.

Time-lapse seismic monitoring of pressure-induced changes in depleting North Sea gas fields reveals that detectable differences in seismic arrival times are observed above the reservoir interval. Geomechanical models of depleting reservoirs predict that, as a result of reservoir compaction from pressure depletion, changes in stress and strain fields occur in the rocks bounding the reservoir (Hatchell et al., 2003).

Forward models of time-lapse time shifts are constructed from stress and strain fields computed using geomechanical models and a stress-strain-dependent seismic velocity (Hatchell and Bourne, 2005b). Based on observations of time-lapse seismic data from several locations around the world, Hatchell and Bourne find that a simple linear model relating seismic velocity with vertical strain works well. Time shifts are computed from the relative velocity changes, which are calculated from the product of vertical strain and velocity-strain coupling coefficient (negative of dilation factor, or $-R$). Their observations also show that velocity-strain dependence is larger for rock elongation than for rock contraction. The former is about five, and the latter is less than half this value. They obtain $-R$ values of 1–3 from empirical velocity-porosity trends and 2–10 using crack models.

Carcione et al. (2007) use two different petroelastic models (asperity deformation and Hertz-Mindlin) at varying effective pressures to show that fractional changes in layer thickness $\Delta L/L$ and seismic velocity $\Delta V/V$ are related linearly. Dilation factor R is negative, and its absolute value is predicted to decrease for shale or increase for sandstone with increasing layer thickness or decreasing effective pressure.

Various investigations document the change in velocities with stress. Wyllie et al. (1958) examine the factors that affect the velocity of ultrasonic signals in porous media. They compare and discuss the data obtained when three cores from the same rock are compressed uniformly, axially, and circumferentially. They find that velocity increases with increasing differential pressure. The increase at first is rapid and then decreases with increasing differential pressure until an approximately constant terminal velocity is attained. Compres-

Manuscript received by the Editor 14 October 2008; revised manuscript received 12 January 2009; published online 26 June 2009.
[1]Colorado School of Mines, Department of Geophysics, Golden, Colorado, U.S.A. E-mail: arpita.bathija@yahoo.com; mbatzle@mines.edu.
[2]Colorado School of Mines, Department of Petroleum Engineering, Golden, Colorado, U.S.A. E-mail: mprasad@mines.edu.

sional V_P and shear V_S velocities are measured by Ball and Batzle (1994) on five sandstone samples as a function of triaxial stress. They find V_P to be controlled primarily by the stress applied parallel to the direction of propagation. Axial and lateral or normal stresses have a strong influence on V_S. Vega (2003) finds similar results on unconsolidated sands.

Sample deformations occurring during these measurements rarely are reported. However, we can estimate the static strains from dynamic velocities by ignoring the differences between static and dynamic elastic properties. Table 1 presents the R values directly reported or extracted from data in previous studies. The major inconsistencies in R values from 4D seismic studies, theoretical modeling, and core analysis are not well understood, as indicated by Janssen et al. (2006).

SAMPLE DESCRIPTION

This is the first laboratory study to report directly the measured R values for sandstones and shale. Table 2 presents the petrological data of all samples used in this study. Samples were prepared with the bedding plane normal to the axial direction. Sample lengths were around 9 cm, and diameters were around 3.75 cm. The shale sample was shorter (4.6 cm) to reduce flow time.

Lyons sandstone

This well-cemented Permian aeolian deposit is composed of rounded grains with a grain size of about 0.2 mm. The grains do not show microcracks, and grain boundaries are not obvious in scanning electron microscope (SEM) images.

Berea sandstone

With a predominantly quartzose framework, this sandstone is fine grained and weakly laminated. The microporosity is associated with authigenic kaolinite and constitutes 10.5% of the total porosity (19%).

Foxhill sandstone

This fine- to medium-grained sandstone has a mean grain size of 0.21 mm. Grains are subangular to rounded and moderately well sorted. Moderate amounts of quartz occur in the framework. Authigenic clay is the dominant clay and is a mixture of kaolinite, chlorite, and smectite. The microporosity constitutes 33% of the total porosity.

North Sea shale

The North Sea shale sample is very fine grained and compacted with a laminated texture. Appropriate procedures for sample han-

Table 1. Review table for dilation factor (R)

$-R$	Data	Stress (MPa)	Method	Lithology	Reference
4:6	R	in situ	4D seismic	Shale	Hatchell & Bourne (2005b)
1:3	R	in situ	4D seismic	Sandstone or carbonate	Hatchell & Bourne (2005b)
1:3	R	—	Velocity-porosity model	—	Hatchell & Bourne (2005b)
2:10	R	—	Microcrack model	—	Hatchell & Bourne (2005b)
4.4:5.4	R	5:40 (differential)	Asperity-deformation model	Shale	Carcione et al. (2007)
2:2.3	R	5:40	Hertz-Mindlin model	Shale	Carcione et al. (2007)
4.25:5	R	5:40	Hertz-Mindlin model	Sandstone	Carcione et al. (2007)
1.5	R	in situ	4D seismic (Valhall field)	Sandstone	Røste et al. (2005)
2.6	R	in situ	4D seismic (Valhall field)	Shale	Røste et al. (2005)
304	Velocity, strain	2.4:8.2 (vertical compressive)	Laboratory uniaxial strain	Finest-grained sands	Vega (2003)
283	Velocity, strain	4.3:10.3	Laboratory uniaxial strain	Fine-grained	Vega (2003)
147	Velocity, strain	2.6:8.1	Laboratory uniaxial strain	Coarse-grained	Vega (2003)
729	Velocity	0.7 (uniaxial)	Laboratory uniaxial stress	Dry Berea sandstone block	Sarkar et al. (2003)
45:40	Velocity	7:14 (differential)	Laboratory hydrostatic stress (North Sea)	Brine-saturated shale cores	Wang (2002)
10:30	R	various	Laboratory (Ekofisk field)	Chalk cores	Janssen et al. (2006)
2	R	in situ	4D seismic (Ekofisk field)	Chalk	Janssen et al. (2006)
4:6	R	in situ	4D seismic (Ekofisk field)	Shale	Janssen et al. (2006)
6:91	R	63:7 (differential) and 7:56 (uniaxial)	Laboratory ultrasonic and deformation	Sandstones	Present study
6.3:10.6	R	49:7 (differential) and 3.5:7 (uniaxial)	Laboratory ultrasonic and deformation	Shale	Present study

dling were developed to preserve the shale in its natural state. For example, exposure to air was minimized by storing the core in mineral oil. The mineral oil was used as a coolant to avoid contact with water-based fluids that could cause unwanted physicochemical reactions during sample preparation (drilling, grinding). Shale's low permeability extended the time needed for the fluid and rock to equilibrate at stress conditions. Hence, mesh screens were placed on the sample to ease fluid flow.

ROCK STRENGTH

The approximate strength of the rock samples was calculated, and stress regimes were developed to ensure that the applied stresses did not lead to sample failure. The maximum uniaxial stress and the differential pressure were constrained by the uniaxial compressive and crushing strength of the rock samples, respectively.

The generalized rock-failure envelopes for sandstones were calculated using Jizba's (1991) relation:

$$\tau = 37(0.36 - \phi)^{1.05}\sigma_n^{0.6}, \qquad (1)$$

where τ and σ_n are the shear and normal stresses at failure, respectively, and φ is porosity. Uniaxial compressive strength C_o was calculated using Jizba's relations, a Dobereiner and DeFreitas (1986) critical porosity value of 0.42 for weak sandstone, and Hoek and Brown's (1980) formulation (Batzle et al., 2006) (equation 2):

$$C_o = -25m + 25[m^2 + 2520 \times (0.42 - \phi)^{2.8}]^{1/2}, \qquad (2)$$

where m is a parameter dependent on lithology ($m = 15$ for sandstones). Equation 2 was verified on the Foxhill sample, which failed as the axial stress reached this rock's uniaxial compressive strength of 16.87 MPa.

The crushing strength C_c was calculated using Zhang's (1991) relation for sands with a grain size of 0.2 mm:

$$C_c = \frac{13.9}{\phi}. \qquad (3)$$

The generalized rock-failure envelopes for shale were calculated using (Dewhurst et al., 2007)

$$\tau = 1.54 + 0.38\sigma_n. \qquad (4)$$

Note that equation 4 is for the North Sea shale with bedding parallel to the axial direction. This equation overestimated the strength because our shale sample had bedding normal to the axial direction.

The value for C_o was calculated using equation 5 (Horsrud, 2001) for the North Sea shale:

$$C_o = 243.6(\phi)^{-0.96}. \qquad (5)$$

No relation was found for calculating C_c for shale; however, we expect this value to be significantly lower than C_c for sandstones.

Table 3 presents calculated C_o and C_c for all samples used in this study using equations 2, 3, and 5.

Table 2. Sample properties

Sample name	Mineral constituents	Plug porosity	Air permeability	Grain density
Units	(%)	(%)		gm/cm^3
Lyons sandstone	Quartz (98)	7.06	0.014 mD	2.48
	Feldspar (2)			
Berea sandstone	Quartz (84.4)	19	200 mD	2.65
	Clay (5.2)			
	Feldspar (4.8)			
	Ankerite (4.8)			
	Siderite (0.4)			
	Calcite (0.3)			
	Mica (0.1)			
Foxhill sandstone	Quartz (73)	24	100 mD	2.48
	Tridymite (12)			
	Clay (10)			
	K-Feldspar (2)			
	Plagioclase (2)			
	Almandite garnet (1)			
North Sea Shale	2:1 Clay + Mica (51)	19	1 nD	2.68
	Kaolinite (16)			
	Opal (16)			
	Quartz (9)			
	Halite (3)			
	Feldspar (2)			
	Pyrite (1)			
	Calcite (1)			
	Siderite (1)			

Table 3. Sample strength

Sample name	C_o	C_c
Units	(MPa)	(MPa)
Lyons sandstone	97.8	197
Berea sandstone	32.8	73
Foxhill sandstone	16.87	57.92
North Sea shale	7.5	—

METHOD

The experimental equipment consisted of a confining-pressure vessel; an axial stress controller; a pressure pump and transfer vessel for controlling pore pressure; a digital oscilloscope; a pulse generator; ultrasonic transducers attached at the top, bottom, and sides of the sample; a data-acquisition device; and a computer. Resistive strain gauges were used to measure deformation (Figure 1).

Velocities were measured in each sample at ultrasonic frequencies (1 MHz) using the pulse transmission technique (Birch, 1960). Flexible epoxy was cast around the sample to prevent hydraulic oil from invading the sample.

Figure 1 shows the axial and radial directions, where stresses were applied and measurements were made. Hydrostatic data were measured when the stresses were equal in all directions (axial stress in the axial direction equal to differential pressure in the radial direction). Uniaxial stress measurements were made while increasing the axial stress at various constant differential pressures. For Berea sandstone, only the velocities and strain parallel to the axial stress direction were measured; for other samples, the velocities and strain parallel and normal to the axial stress direction were measured. The axial $V_{S\parallel}$ and radial $V_{S\perp}$ shear velocities were polarized radially. The direction parallel to the axial stress direction is referred to as axial and the normal direction as radial.

The data used in this study were measured while downloading differential pressure (Figure 2). Figure 3 shows the measurement space over which the data were collected for each sample. The stress space is different for the samples because of the difference in their strengths. The differential pressure was decreased from 63 MPa (Berea and Lyons sandstones) and 49 MPa (Foxhill sandstone, North Sea shale) to 7 MPa. At each differential pressure, the axial stress values were varied from the differential pressure value to 63 MPa for Berea and 49 MPa for Foxhill and North Sea shale. The value K refers to a constant ratio of differential pressure to axial stress.

To account for pore pressure in the brine-saturated cases, differential pressure ($P_d = P_c - P_p$) and differential axial stress ($P_a - P_p$) were used with P_c the confining pressure, P_p the pore pressure, P_a the axial stress, and P_d the differential pressure. Because P_p is zero for the dry cases, confining pressure is the same as differential pressure and axial stress is the same as differential axial stress. For shale, only brine-saturated data were collected, because special care was taken to keep the sample in its natural state as far as possible. This stress-state matrix is a more general acquisition method and allows analyses along arbitrary stress paths (with $P_a > P_c$) as compared to most studies, which collect data only along specific stress paths.

The length changes were measured by the foil-resistance strain gauges attached to the sample in the axial and radial directions. The Wheatstone bridge principle was used for more accurate measurements of length changes. The calibrated microstrain value was computed using

$$\mu\epsilon_{\text{cal}} = \left[\frac{1}{\text{G.F.}}\right]\left[\frac{R_g}{R_{\text{cal}} + R_g}\right] \times 10^6, \tag{6}$$

where $\mu\epsilon_{\text{cal}}$ is calibrated microstrain, G.F. is gauge factor, R_g is gauge resistance, and R_{cal} is shunt resistance (Measurements Group, Inc. (16 July 2007); Measurements Group, Inc. (2 March 2007); Measurements Group, Inc. (16 July 2007); Micro-Measurements

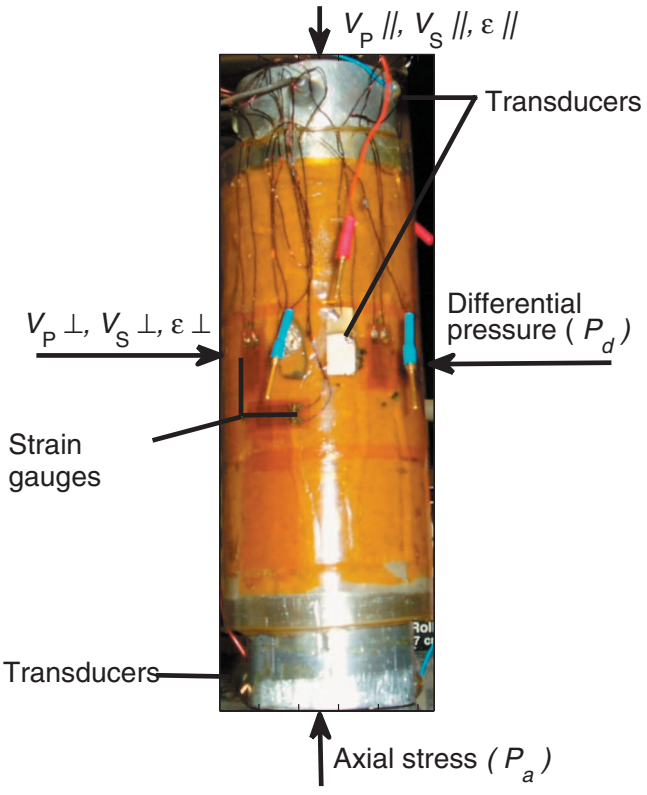

Figure 1. Photograph of the Foxhill sample with strain gauges and transducers attached to measure the deformation and velocities. The values $V_{P\parallel}$, $V_{S\parallel}$, $\epsilon_\parallel$ and $V_{P\perp}$, $V_{S\perp}$, $\epsilon_\perp$ are with respect to the axial stress direction.

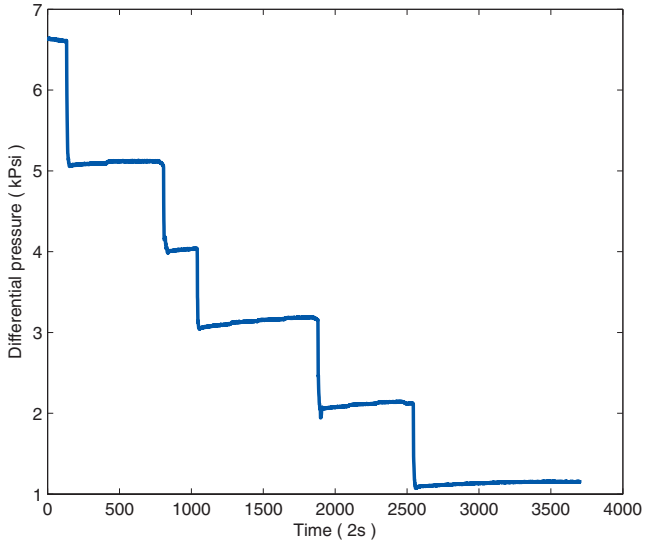

Figure 2. Strain and ultrasonic velocities in this study correspond to downloading differential pressure. The unit of time in the x-axis of the plot is 2 s; the pressure in the y-axis is 1000 psi (kpsi).

(3 September 2003)). The measured change in voltage was calibrated to obtain the microstrain data using

$$\mu\epsilon = \left[\frac{\mu\epsilon_{\text{cal}}}{\Delta\text{vol}_{\text{cal}}}\right]\Delta\text{vol}, \tag{7}$$

where $\mu\epsilon$ is microstrain, $\Delta\text{vol}_{\text{cal}}$ is calibrated change in voltage, and Δvol is change in voltage.

The velocities and Young's modulus were measured on an aluminum sample to calibrate the equipment setup. Each reading (ultrasonic velocity) was taken after the strain values had stabilized (about 10 minutes in sandstones and 2 hours in shale). The samples were saturated under pressure for 12 hours with 30,000 ppm sodium chloride (NaCl) for sandstones and for 48 hours with 50,000 ppm potassium chloride (KCl) for shale.

Velocity was computed as the quotient of the length of the sample and the traveltime. The value R was calculated by finding the ratio of the change in velocity over initial velocity to strain:

$$R = \frac{\frac{\Delta V}{V}}{\epsilon}, \tag{8}$$

where ϵ is strain in the direction of velocity measurement. Strain is the dimensionless ratio of change in length with respect to original length $[\Delta L/L]$ and is considered to be negative for compression/compaction and positive for tension/elongation in this study. Note that R is always negative because velocity decrease is associated with sample elongation and velocity increase is associated with sample compaction.

The static Young's modulus was obtained from uniaxial stress data, where the axial stress was increased at constant differential pressures. Young's modulus E_s is the slope of the stress-strain curve:

$$E_s = \frac{d\sigma_{zz}}{d\epsilon_{zz}}, \tag{9}$$

where $d\sigma_{zz}$ is the incremental axial stress and $d\epsilon_{zz}$ is the strain change along the same zz-direction as the axial stress. In our study, $d\sigma_{zz}$ refers to $[P_a - P_c]$ and $d\epsilon_{zz}$ refers to $[\epsilon_{\|P_a>P_c} - \epsilon_{\|P_a=P_c}]$.

The dynamic Young's modulus was computed using

$$E_d = \frac{\rho V_S^2[3V_P^2 - 4V_S^2]}{V_P^2 - V_S^2}, \tag{10}$$

where ρ is the density of the rock and where V_P and V_S are compressional and shear velocities, respectively. In our study, V_P and V_S refer to $V_{P\|}$ and $V_{S\|}$, respectively, because those are parallel to the axial stress direction.

Thomsen (1986) anisotropic parameters ε and γ (equations 11 and 12) are defined as

$$\varepsilon \approx \frac{V_{P\|} - V_{P\perp}}{V_{P\perp}} \tag{11}$$

and

$$\gamma \approx \frac{V_{S\|} - V_{S\perp}}{V_{S\perp}}, \tag{12}$$

where $V_{P\perp}$ is the compressional and $V_{S\perp}$ is the shear velocity normal to the axial stress direction, $V_{P\|}$ is the compressional velocity parallel to the axial stress direction, and $V_{S\|}$ is the shear velocity parallel to the axial stress direction and polarized parallel to the bedding plane.

Uncertainty analysis

To find the uncertainties in velocity and strain measurements, we used the following for propagation of uncertainty:

$$\delta q = \sqrt{\left[\frac{\partial q}{\partial x}\delta x\right]^2 + \cdots + \left[\frac{\partial q}{\partial z}\delta z\right]^2}, \tag{13}$$

where $x,\ldots,z$ are measured with uncertainties $\delta x,\ldots,\delta z$ (which are independent, random, and small) and the function $q(x,\ldots,z)$ is computed from the measured values with uncertainty δq (Taylor, 1939). The relative uncertainty is defined as the ratio of uncertainty in a measured value with respect to the measured value $\delta x/x$.

Relative uncertainty involved in handpicking first-arrival traveltimes was $\pm 1\%$. The relative uncertainty in length was assumed to be the strain value measured to account for the corrections in velocity because of change in length. Applying equation 13, we calculated uncertainty in velocity and plotted it as error bars in Figure 4.

The relative uncertainty in strain was calculated to be $\pm 0.5\%$ by applying equation 13 to equation 6. The relative uncertainty in R was the same as the relative uncertainty in strain because the uncertainties in the velocities compensate each other (equation 8). The error bars are contained in the size of the symbols for R.

These are measurement uncertainties, and they do not include systematic errors or biases such as sample heterogeneity or bad gauge mounting. However, the errors were assumed to be negligible in our

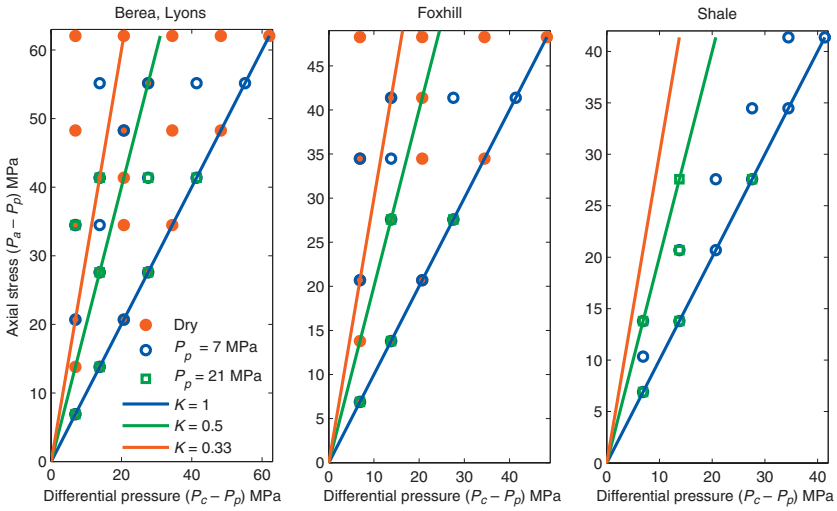

Figure 3. Measurement states for (a) Berea and Lyons sandstone, (b) Foxhill sandstone, and (c) North Sea shale. Each point represents a location in stress space where velocities were measured. Deformation in the sample was recorded continuously throughout the experiment. The value K refers to a constant ratio of differential pressure to axial stress. The hydrostatic line for equal stresses with $K = 1$ is shown in blue. Nonhydrostatic lines with $K = 0.5$ (green) and $K = 0.33$ (red) are also shown.

experiments because of the calibration procedure on aluminum sample and averaging strains at the opposite ends of the rock samples.

RESULTS

This section describes the components of R such as ultrasonic velocities, attributes calculated from static and dynamic moduli, and anisotropy parameters. The dilation factor and its components are discussed separately to better understand the dependence of R on different rock types, fluid, and stress as they complement and/or validate each other.

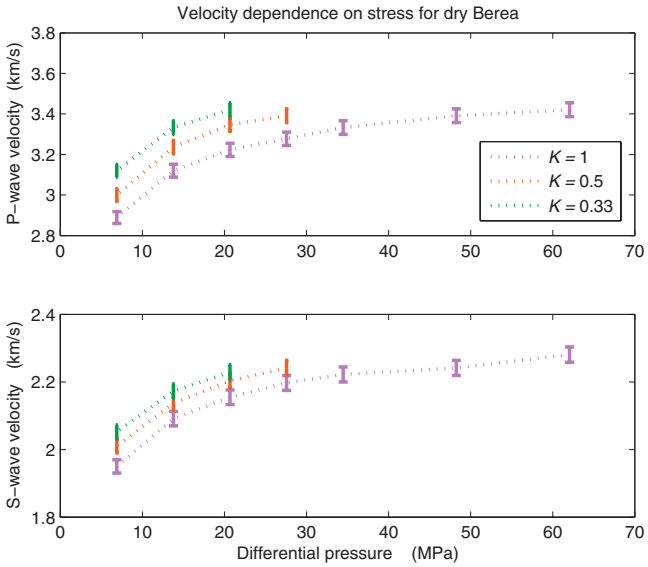

Figure 4. Velocity paths under hydrostatic and nonhydrostatic stresses for dry Berea sandstone. The value K refers to a constant ratio of confining pressure to axial stress. For example $K = 1$ implies a hydrostatic stress state. The uncertainties in measurement of velocity are plotted as error bars. The velocity paths are different for hydrostatic and both nonhydrostatic conditions.

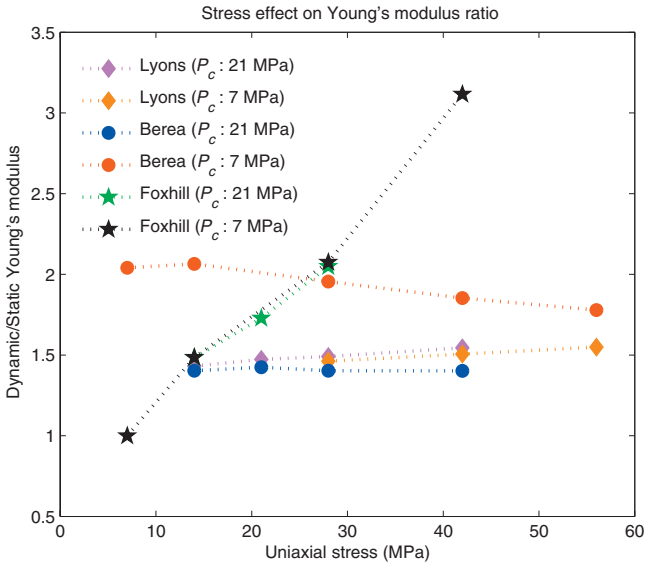

Figure 5. Dynamic/static Young's modulus. The ratio of dynamic to static Young's modulus varies from 1 to 3.1 for sandstones and remains approximately constant for Berea and Lyons samples. However, this ratio dramatically increases with increase in uniaxial stress for the Foxhill sandstone. The modulus ratio is a function of the change in crack content with stress.

Static versus dynamic

Static (macroscopic and isothermal) elastic moduli generally are equal to or less than the dynamic (adiabatic) moduli (Simmons and Brace, 1965; Jizba et al., 1990; Zimmer, 2003; Olsen et al., 2008). The difference between static and dynamic moduli is related more to the amplitude of the measurement than to the frequency. Very-low-amplitude ultrasonic waves are not expected to cause rotation or frictional sliding along grain boundaries and therefore sense only open-pore-space compliance. There is lack of rigor in the large strains computed from small-strain velocities in the dynamic measurements, making the rock appear less compliant.

The ratio of dynamic bulk moduli to static bulk moduli depends strongly on confining pressure (Jizba, 1991; Zimmer, 2003). The ratio of dynamic bulk moduli to static bulk moduli in tight gas sandstones varies from one to three (Jizba, 1991), depending on shale content and confining pressure. The ratio of dynamic to static Young's modulus for reservoir chalks varies from 1.3 to five (Olsen et al., 2008). Our ratio for dynamic-to-static Young's modulus also varies from 1.0 to 3.1 for sandstones (Figure 5).

The ratio of dynamic to static Young's modulus remains approximately constant for Berea and Lyons sandstones. However, this ratio dramatically increases with increase in uniaxial stress for Foxhill samples. The modulus ratio is a function of the change in crack content with stress. We define cracks as compliant pores, which can be described as having lower aspect ratio. Aspect ratio is the ratio of the minor to the major axis of an elliptical pore. Thus, thin, open pore spaces between distributed grain boundaries are referred to as cracks. The increased uniaxial stress in Foxhill sandstone probably generates more open cracks because the strength of this high-porosity sandstone is much lower than the other two sandstones (Table 3). An increase in stiffness from decrease in porosity in the different samples is evident in Figure 6. Increasing stiffness at higher confin-

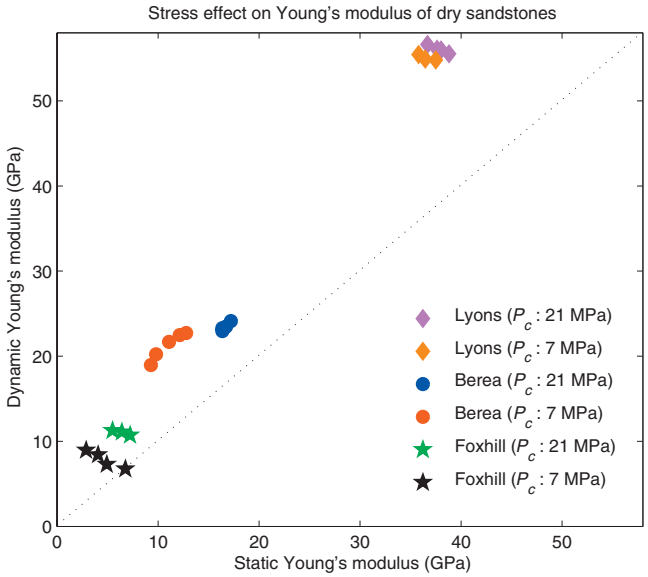

Figure 6. Static versus dynamic Young's modulus. Increasing stiffness with lower porosity and higher confining pressure P_c is evident.

ing pressures is seen in all of the sandstone samples in Figure 6 because of the closure of cracks.

The static Young's modului obtained for our North Sea shale were 2.6–5 GPa. The static Young's modulus of fresh Ashfield shale varied from 2.7 to 4.9 GPa (Ghafoori et al., 1993) using direct shear, triaxial, and uniaxial compressive strength (UCS) tests, which agree closely with our values. Values of the static Young's modulus for North Sea shales from various depths ranged from 0.8 to 12.2 GPa (Horsrud et al., 1998) using undrained triaxial tests. Our values fall within this range.

Velocity

The velocity increase with pressure shows typical rapid increase at low pressures followed by a flattened curve at higher pressures (Wyllie et al., 1958; Ball and Batzle, 1994; Zimmer, 2003). Presumably, cracks close at higher pressure, and velocities approach a relatively constant velocity. The data collected along $K = 1$ (hydrostatic or equal stresses, $P_a = P_c$), $K = 0.5$ (nonhydrostatic, $P_a = 2P_c$), and $K = 0.33$ (nonhydrostatic, $P_a = 3P_c$), when plotted as a function of confining or differential pressure, show that the velocity paths (Figure 4) differ for hydrostatic and both nonhydrostatic conditions. This is true for all of the samples in dry as well as brine-saturated cases, but only the dry Berea case is shown in Figure 4.

The amount of change in velocity with change in hydrostatic pressure is a qualitative measure of the number of cracks. This is consistent with the fact that the crack content in Foxhill sandstone is highest among the sandstones, which makes it more stress sensitive than Berea or Lyons samples (Figure 7).

Velocity surfaces were calculated from the matrix of velocities measured over axial and differential pressure conditions (Figure 3). Contours of equal velocity were then plotted in Figures 8–10. These contours make it easier to see the contrasting dependence on stresses for V_P and V_S. Note that V_S drops dramatically with saturation. The velocity drop indicates some form of chemical frame softening (Adam et al., 2006) because it cannot be explained by density increase alone.

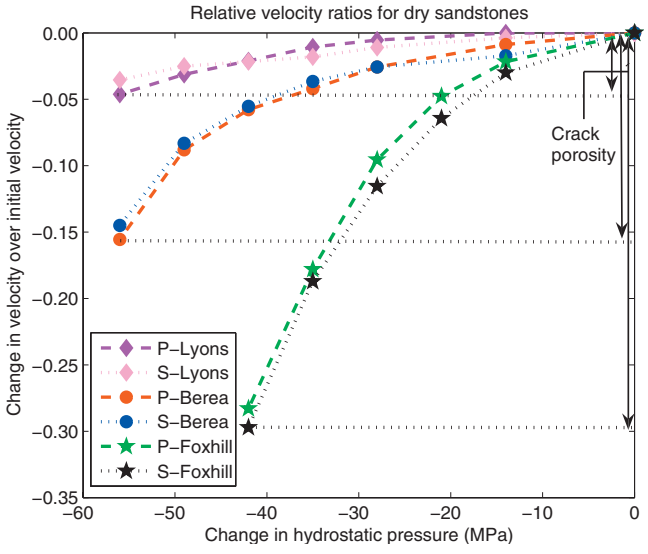

Figure 7. Changes in velocities over initial velocity plotted against change in hydrostatic pressure to find the qualitative influence of crack porosity in sandstones. The crack content in Foxhill sandstones is highest among the sandstones, which makes it more stress sensitive than Berea or Lyons sandstone.

Anisotropy

For dry Berea sandstone, the P-wave velocity contours (Figure 8) show that the axial V_P is more sensitive to axial stress than to differential or confining pressure. In our Berea sample, this may be because of horizontal bedding, which generally means open horizontal cracks. This sensitivity of V_P to axial stress is reduced more in the

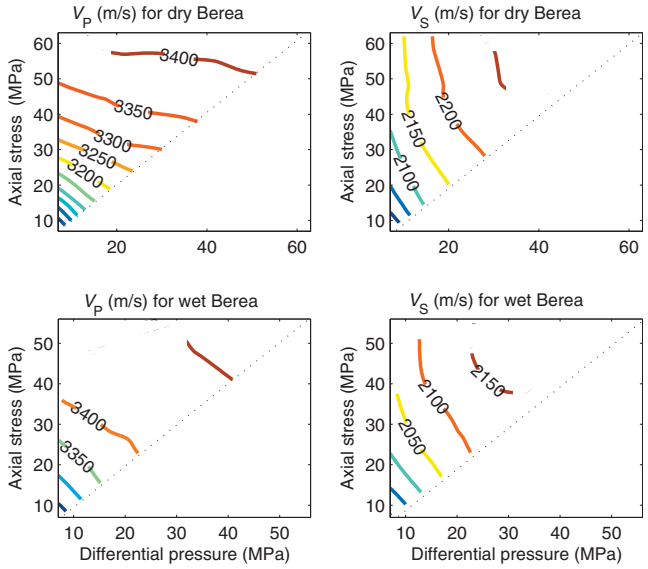

Figure 8. Axial velocity contours for dry and brine-saturated Berea sandstone. The axial V_P is more sensitive to the axial stress than to differential pressure in dry P-wave velocity contours. See Figure 3 for the specific points of measurement.

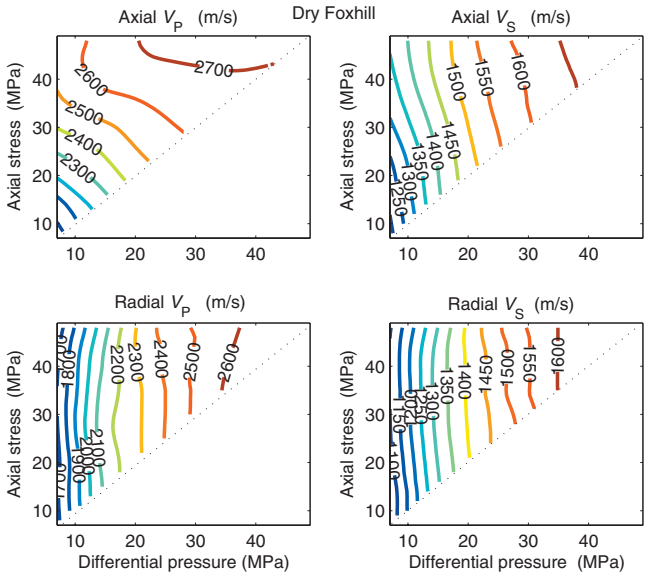

Figure 9. Axial and radial velocity contours for dry Foxhill sandstone. Radial P-wave velocity is more sensitive to differential pressure than to axial stress.

brine-saturated cases than in the dry case, probably because the cracks are filled with less compressible fluid, making the velocities more isotropic.

For dry Foxhill sandstone, the P-wave velocity contours (Figure 9) show that the radial V_P is more sensitive to the differential or confining pressure than axial V_P. This is consistent with a wave being most sensitive to cracks when its direction of propagation or direction of polarization is normal to the crack faces. Hatchell and Bourne (2005b) show that vertical P-wave velocity is four times more sensitive to the presence of horizontal than vertical cracks using a theoretical crack model (Sayers and Kachanov, 1995). Therefore, our Foxhill sample might be having a larger population of axially oriented cracks. Sensitivity of axial V_S (polarized normal to the axial cracks) to differential pressure in the brine-saturated case is reduced in comparison to the dry case (Figure 10).

The Thomsen (1986) anisotropy parameters ε and γ show that crack-induced anisotropy increases with axial stress, and this increase is more pronounced at lower confined stress states (Figure 11). Sarkar et al. (2003) and Fuck et al. (2007) also demonstrate that the time-lapse changes of anisotropy can provide useful information about temporal variations in the stress field.

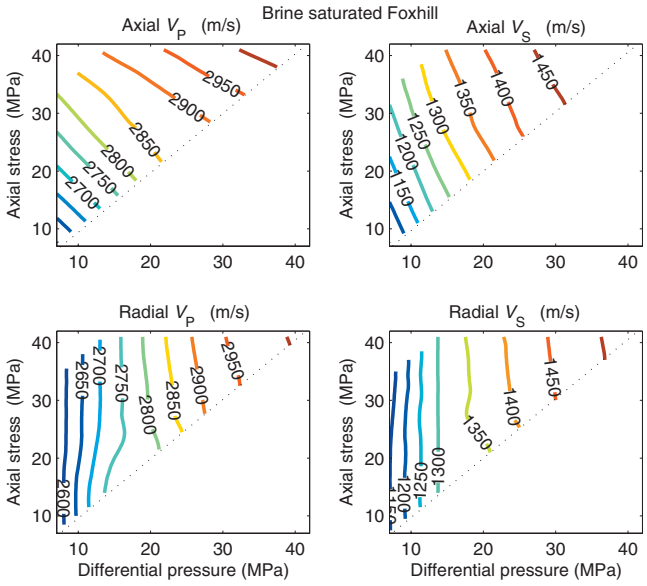

Figure 10. Axial and radial velocity contours for brine-saturated Foxhill sandstone. Axial V_S in the brine-saturated case is less sensitive to differential pressure compared to the dry case.

Dilation factor

A decrease in hydrostatic stress results in a decrease in all velocities. The magnitude of relative velocity change increases as a result of increased stress sensitivity of the velocity, owing to a larger number of open cracks at low pressures. These cracks result in smaller strains in comparison to the relative change in velocities at low pressures in sandstones. Hence, the absolute R values are higher at lower pressures (see Figure 12) for all sandstones. The R values decreased with decreasing confining pressure for shales. Shales mostly have cracks and few high-aspect-ratio pores. The shale sample shows significantly larger strain than the sandstones, and this strain reduces with higher pressures (Figure 13). At higher pressures, relative velocity changes are greater than strain because shales lack high-aspect-ratio pores. This behavior is also supported by the model calculations (Holt et al., 2005; Carcione et al., 2007).

The absolute R values decrease with saturation for P-waves (Figure 14). This is because a fluid makes the rock stiffer as its cavities are filled with less compressible fluid. The stiffness makes the saturated rock less stress sensitive. Greater stress sensitivity at lower differential pressures leads to higher absolute R values.

Figure 15 show the component of R, i.e., change in velocity over initial velocity changes with uniaxial stress increments. Velocity increases in the direction parallel to axial stress, probably from crack closure, and it increases with uniaxial stress. There is velocity decrease from elongation in the direction normal to the axial stress direction, but it is almost constant.

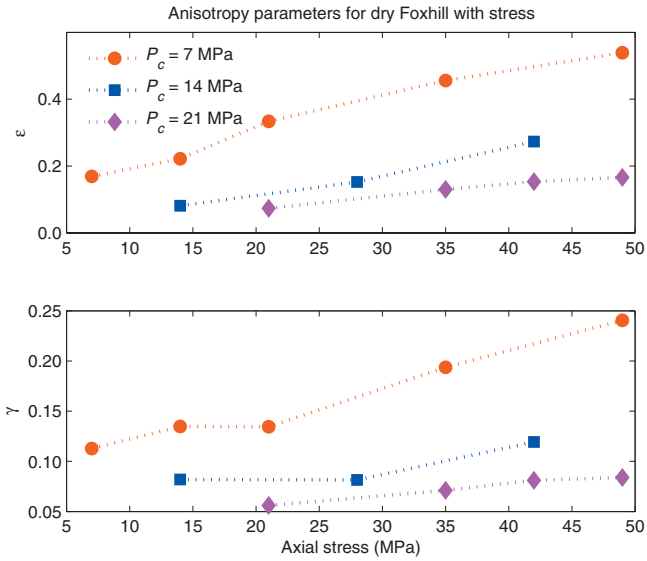

Figure 11. Anisotropy parameters plotted as a function of axial stress. Crack-induced anisotropy increases with axial stress. This increase is greater at lower confined stress states.

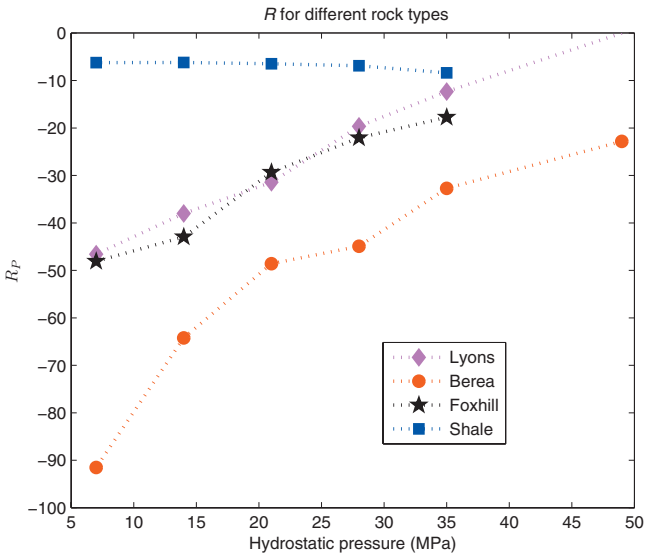

Figure 12. R values are plotted as a function of hydrostatic pressure. At the lowest hydrostatic pressure, absolute R value is the highest for sandstones and lowest for shale.

Figure 16 shows the strain changes with uniaxial stress increments. Strains parallel to the axial stress direction are compaction (negative strain) and increase with uniaxial stress. Elongation, in the direction normal to axial stress direction in Foxhill sandstone, also increases with uniaxial stress.

A uniaxial stress increase results in a decrease in absolute R values of the waves propagating (or being polarized for shear waves) along the applied stress direction. These absolute R values of the waves propagating (or being polarized for shear waves) normal to this direction are also reducing, as seen in Figure 17. This is probably because a compressive stress component normal to a crack face may close the crack, increasing the velocities, but the length changes are larger than velocity changes. If large shear stress is applied, new cracks primarily aligned with the maximum principal stress might be generated. Here again, length changes are larger than velocity changes. Holt et al. (2005) support this behavior using model calculations.

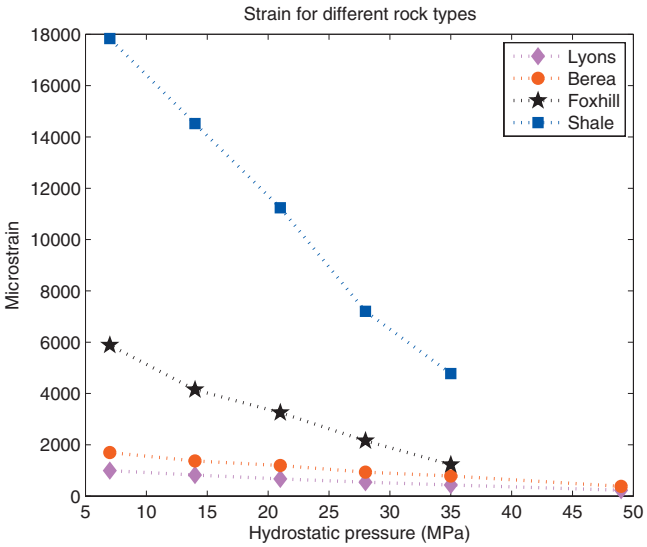

Figure 13. Strain as a function of hydrostatic pressure. The samples increase in size as the hydrostatic pressure is decreased. The shale sample shows significantly larger deformation in comparison to the sandstones.

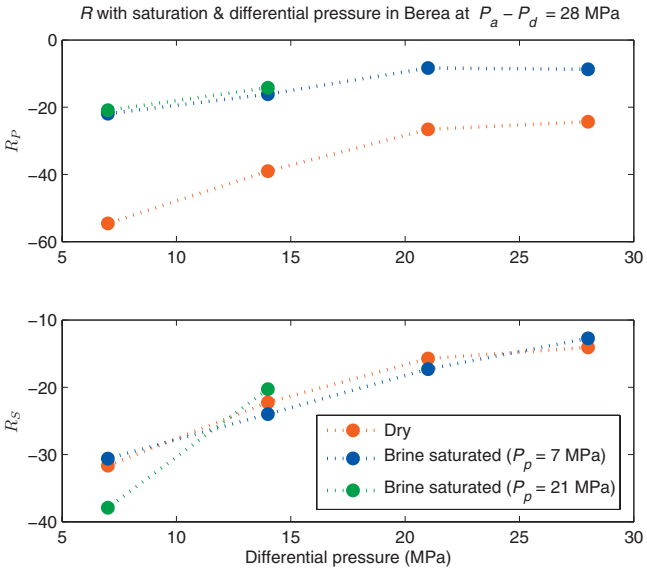

Figure 14. The R values with fluid saturation and differential pressure at a constant difference between the axial stress and the differential pressure in Berea sandstone. Absolute R_P value decreases with fluid saturation and increasing differential pressure; R_S is insensitive to fluid saturation.

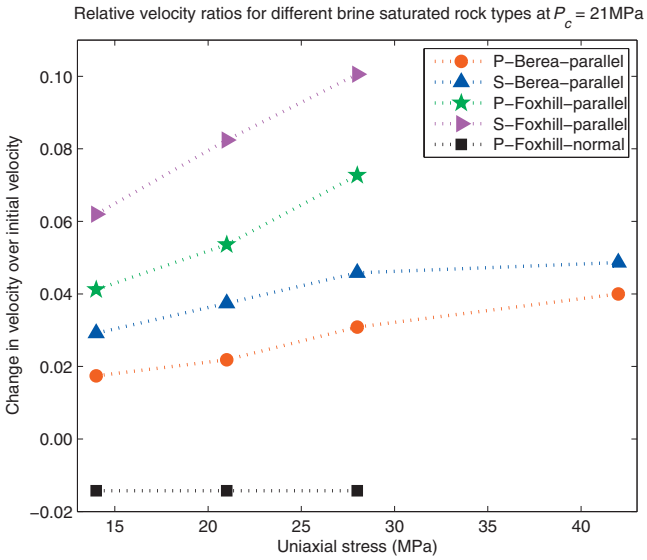

Figure 15. Change in velocities over initial velocity as a function of uniaxial stress. There is velocity increase in the direction parallel to uniaxial stress, probably because of crack closure, and it increases with uniaxial stress. There is velocity decrease from elongation in the direction normal to the axial stress direction, but it is almost constant.

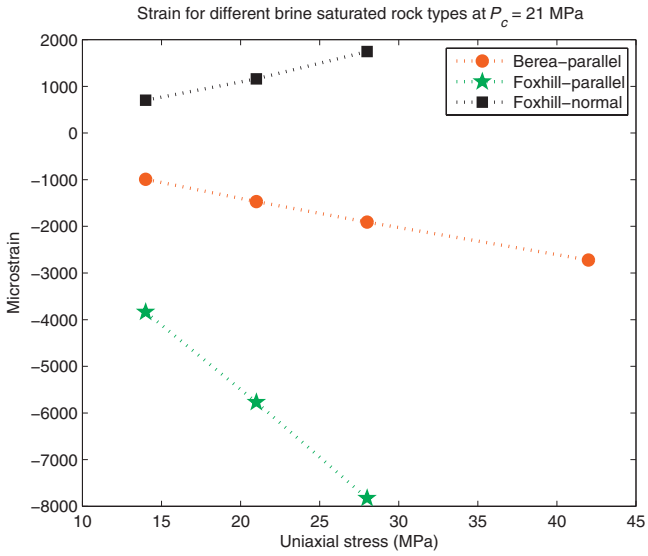

Figure 16. Strain with uniaxial stress. Strains parallel to the axial stress direction are compaction (negative strain) and increase with uniaxial stress. There is elongation in the direction normal to axial stress direction in Foxhill sandstone. Elongation also increases with uniaxial stress.

R-value comparison

Janssen et al. (2006) compare R values calculated from 4D seismic data, velocity-porosity trends, and core analyses. Their core experiments from the Ekofisk reservoir, which is mostly chalk ($-R$ = 10 to 30), also show much larger stress sensitivity for R than what is observed in seismic data or is predicted from rock-physics trends.

In time-lapse seismic data, the velocities correspond to the dynamic mechanism, but strain is inferred from static mechanisms, such as seafloor subsidence and reservoir compaction (Hatchell and Bourne, 2005a; Røste et al., 2005):

$$\Delta t = (1 - R)\epsilon_{zz}t, \tag{14}$$

where Δt is time-lapse time shifts, ϵ_{zz} is vertical strain, and t is traveltime for normal-incidence vertical P-waves. Theoretical models that use rock-property trends derived from velocity-porosity regression, microcrack model, asperity-deformation models, and Hertz-Mindlin models (Hatchell and Bourne, 2005b; Røste et al., 2005; Carcione et al., 2007) use the same dynamic mechanism to calculate the change in velocities and strains. Hence, comparing modeled R values with the 4D seismic data is inconsistent. New models need to be developed.

Numerous investigations document the change in velocities with increasing stress. However, the sample deformations occurring during these measurements rarely are reported. We can estimate the static strains from dynamic velocities by ignoring the differences between static and dynamic elastic properties. To calculate R from dynamic measurements, we first calculate the dynamic Young's modulus values from the acoustic velocities using equation 10. The strain is calculated using equation 9, making the assumption that static and dynamic Young's moduli are the same. Then R is computed using equation 8.

For example, an estimated R of -739 was extracted when a block of Berea sandstone was subjected to a uniaxial stress of 6 MPa parallel to the bedding plane in an unconfined, dry condition (Sarkar et al., 2003). This is compared with our R value of -100 (dynamic strain) and -58 (static strain) for a uniaxial stress increase of 7 MPa in a Berea sample. Because the axial stress was applied normal to the bedding plane in our study, we saw much higher strains and therefore lower R values. The difference in R also can be explained by the fact that the Berea block of Sarkar et al. (2003) was subjected to uniaxial stress in an unconfined state, whereas our sample was subjected to uniaxial stress at 7 MPa confined stress.

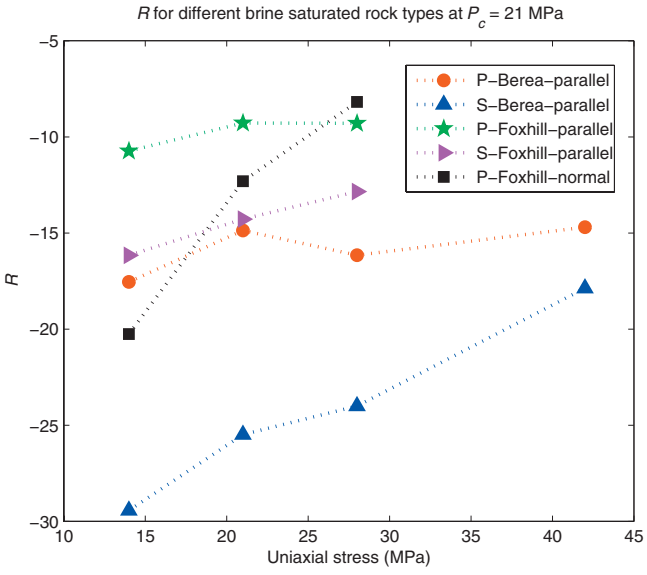

Figure 17. The R values as a function of uniaxial stress at a constant differential pressure P_d of 14 MPa($=21(P_c) - 7(P_p)$). Parallel and normal are with respect to the axial stress direction. Notice the large crack-induced anisotropy in the R values for Foxhill sandstone.

Our R values for the North Sea shale varied from -8.5 to -6 with hydrostatic pressure decrease and -11 to -6 with uniaxial stress increments. The dynamic R values extracted from Wang (2002) are higher than our R values for shales. Shales mostly have lower-aspect-ratio pores, so we expect that dynamic mechanism does not represent them correctly.

CONCLUSIONS

We found R values to be strongly dependent on the stress states; hence, using a constant value of R from the surface (unconfined stress state) to the reservoir depth (higher confined stress state) should be avoided. Reduced stress sensitivities of velocities at higher confining pressure and greater strain (from higher-aspect-ratio pores closing) lead to lower absolute values of R in sandstones. The absolute R values for P-waves were lower for fluid-filled rocks because the presence of fluid makes the rock stiffer. The R values were different for P- and S-waves, especially in the presence of fluids. Because PS converted waves are used in 4D monitoring, using the same value of R for P- and S-waves can lead to errors in assessing production-related changes.

We found that R values depend on the density of cracks and their alignment with respect to the stress direction. Intrinsic anisotropy and stress-induced crack anisotropy play important roles in understanding R, although crack-induced anisotropy is lower at higher confining pressures and in fluid-filled rocks.

The dynamic Young's modulus generally is higher than the static Young's modulus. The ratio of dynamic to static moduli increases in crack-dominated rocks at lower confining pressures. For high-aspect-ratio pore-dominated rocks, the ratio of dynamic to static Young's moduli almost remains constant with increasing uniaxial stress. In rocks with a higher density of cracks parallel to the axial stress direction, this ratio increases with uniaxial stress increments. The ratio should decrease if there is a higher density of cracks normal to the axial stress direction.

The R values are dependent on the deformation mechanisms controlling the strain. Hence, comparing the theoretical models based on rock-property trends with 4D seismic data is inconsistent because none of the models calculates the strain from static deformation mechanism.

This study shows that absolute R values increase for sandstones and decrease for shales with decreasing confining pressure. These trends match with modeled R values for sandstones and shales in earlier studies. Lower values of R from 4D seismic data can be explained by the fact that 4D seismic data see the combined effect of the overburden (mostly shales) and reservoir (sandstones) rocks. Fluid-filled reservoir rocks, buried deep in the earth (higher confining pressures), lead to lower absolute values of R. The overburden occupies a larger area than the reservoir, leading to a dominant role. Lowering R values for shales with decreased confining pressure will probably reduce R further if the confining pressure decreases as we move up to the surface from just above the reservoir.

Our data not only offer insight into the behavior of R values with different rock types, stress, and fluid, but they also can be used to constrain model calculations.

ACKNOWLEDGMENTS

We acknowledge Bob Kranz for many useful insights. We appreciate help from Matthew Wisniewski, Trevor Irons, Joey Cohrs, Ryan Paynter, and Weiping Wang in the laboratory. We would like to thank Ilya Tsvankin, Luis Tenorio, Ning Lu, and Richard Wendlandt for their feedback and discussions. We appreciate all the help from the reviewers and editors to improve the manuscript. We thank the Petroleum Research Fund (PRF 43596-AC8), the Clay Minerals Society, the Norwegian Research Council (Award 2007/9098-LIGU), and the Fluids Consortium for financial support.

REFERENCES

Adam, L., M. Batzle, and I. Brevik, 2006, Gassmann's fluid substitution and shear modulus variability in carbonates at laboratory seismic and ultrasonic frequencies: Geophysics, **71**, no. 6, F173–F183.

Ball, V., and M. Batzle, 1994, Contrasting stress dependence of compressional and shear velocities: Implications for laboratory, logging, and seismic measurements: 64th Annual International Meeting, SEG, Expanded Abstracts, 1065–1068.

Batzle, M., D. Han, and R. Hofmann, 2006, Rock properties, *in* J. Fanchi ed., Petroleum engineering handbook: Society of Petroleum Engineers, 571–685.

Birch, F., 1960, The velocity of compressional waves in rocks to 10 kilo bars, part 1: Journal of Geophysical Research, **65**, 1083–1102.

Carcione, J., M. Landrø, A. Gangi, and F. Cavallini, 2007, Determining the dilation factor in 4D monitoring of compacting reservoirs by rock-physics models: Geophysical Prospecting, **55**, no. 6, 793–804.

Dewhurst, D., A. Siggins, M. Clennell, M. Raven, and H. Nordgård-Bolås, 2007, The ultrasonic response of North Sea Shale to undrained loading: 77th Annual International Meeting, SEG, Expanded Abstracts, 1525–1529.

Dobereiner, L., and M. DeFreitas, 1986, Geotechnical properties of weak sandstones: Geotechnique, **36**, 79–94.

Fuck, R., A. Bakulin, and I. Tsvankin, 2007, Theory of traveltime shifts around compacting reservoirs: 3D solutions for prestack data: 77th Annual International Meeting, SEG, Expanded Abstracts, 2929–2933.

Ghafoori, M., M. Mastropasqua, J. Carter, and D. Airey, 1993, Engineering properties of Ashfield Shale, Australia: Bulletin of Engineering Geology and the Environment, **48**, no. 1, 43–58.

Hatchell, P., and S. Bourne, 2005a, Measuring reservoir compaction using time-lapse timeshifts: 75th Annual International Meeting, SEG, Expanded Abstracts, 2500–2503.

———, 2005b, Rocks under strain: Strain-induced time-lapse time shifts are observed for depleting reservoirs: The Leading Edge, **24**, 1222–1225.

Hatchell, P. J., A. van den Beukel, M. M. Molenaar, K. P. Maron, C. J. Kenter, J. G. F. Stammeijer, J. J. van der Velde, and C. M. Sayers, 2003, Whole earth 4D: Reservoir monitoring geomechanics: 73rd Annual International Meeting, SEG, Expanded Abstracts, 1330–1333.

Hoek, E., and E. T. Brown, 1980, Underground excavations in rock: Taylor and Francis.

Holt, R., O.-M. Nes, and E. Fjaer, 2005, In-situ stress dependence of wave velocities in reservoir and overburden rocks: The Leading Edge, **24**, 1269–1274.

Horsrud, P., 2001, Estimating mechanical properties of shale from empirical correlations: SPE Drilling Completion, **16**, 68–73.

Horsrud, P., E. Sønstebø, and R. Bøe, 1998, Mechanical and petrophysical properties of North Sea shales: International Journal of Rock Mechanics and Mining Sciences, **35**, 1009–1020.

Janssen, A., B. Smith, and G. Byerley, 2006, Measuring velocity sensitivity to production-induced strain at the Ekofisk field using time-lapse time shifts and compaction logs: 76th Annual International Meeting, SEG, Expanded Abstracts, 3200–3204.

Jizba, D., 1991, Mechanical and acoustical properties of sandstones and shales: Ph.D. dissertation, Stanford University.

Jizba, D., G. Mavko, and A. Nur, 1990, Static and dynamic moduli of tight gas sandstone: 60th Annual International Meeting, SEG, Expanded Abstracts, 827–829.

Measurements Group, Inc., undated, Bondable resistance temperature sensors and associated circuitry: Technical Note TN-506, http;//www.vishag-.com/strain-gages/knowledge-base-list/technotes-list, accessed 16 July 2007.

———, undated, Errors due to Wheatstone bridge nonlinearity: Technical Note TN-507, http;//www.vishag.com/strain-gages/knowledge-base-list/technotes-list, accessed 2 March 2007

———, undated, Shunt calibration of strain gage instrumentation: Technical Note TN-514, http;//www.vishag.com/strain-gages/knowledge-base-list/technotes-list, accessed 16 July 2007.

Micro-Measurements, undated, Temperature sensors and LST matching networks: Product Bulletin PB-105, http;//www.vishag.com/strain-gages/knowledge-base-list/technotes-list, accessed 3 September 2007.

Olsen, C., H. Christensen, and I. Fabricius, 2008, Static and dynamic Young's modulus of chalk from the North Sea: Geophysics, **73**, no. 2, E41–E50.

Røste, T., A. Stovas, and M. Landrø, 2005, Estimation of layer thickness and velocity changes using 4D prestack seismic data: Ph.D. dissertation, Norwegian University of Science and Technology (NTNU).

Sarkar, D., A. Bakulin, and R. Kranz, 2003, Anisotropic inversion of seismic data for stressed media: Theory and a physical modeling study on Berea sandstone: Geophysics, **68**, no. 2, 690–704.

Sayers, C., and M. Kachanov, 1995, Microcrack-induced elastic wave anisotropy of brittle rocks: Journal of Geophysical Research, **100**, 4149–4156.

Simmons, G., and W. Brace, 1965, Comparison of static and dynamic measurements of compressibility of rocks: Journal of Geophysical Research, **70**, 5649–5656.

Taylor, J., 1939, An introduction to error analysis: The study of uncertainties in physical measurements: University Science Books.

Thomsen, L., 1986, Weak elastic anisotropy: Geophysics, **51**, 1954–1966.

Vega, S., 2003, Intrinsic and stress-induced velocity anisotropy in unconsolidated sands: Ph.D. dissertation, Stanford University.

Wang, Z., 2002, Seismic anisotropy in sedimentary rocks, part 2: Laboratory data: Geophysics, **67**, 1423–1440.

Wyllie, M., A. Gregory, and G. Gardner, 1958, An experimental investigation of factors affecting elastic wave velocities in porous media: Geophysics, **23**, 459–493.

Zhang, J.-X., 1991, Mechanical compaction and the brittle ductile transition in porous rocks: Geological implications for accretionary wedge seismicity: Ph.D. dissertation, State University of New York at Stony Brook.

Zimmer, M., 2003, Seismic velocities in unconsolidated sands: Measurements of pressure, sorting and compaction effects: Ph.D. dissertation, Stanford University.